Analytical solution of a mass-spring system containing shape memory alloys

Effects of nonlinearity and hysteresis

Zhuo, Mingzhao; Xia, Minglu; Sun, Qingping

Important note
To cite this publication, please use the final published version (if applicable).
Please check the document version above.

Analytical solution of a mass-spring system containing shape memory alloys: Effects of nonlinearity and hysteresis

Mingzhao Zhuo[a,b], Minglu Xia[a], Qingping Sun[a,*]

[a]Department of Mechanical and Aerospace Engineering, The Hong Kong University of Science and Technology, Hong Kong
[b]Faculty of Civil Engineering and Geosciences, Delft University of Technology, Delft, the Netherlands

Abstract

Nonlinear dynamics of vibration systems containing NiTi shape memory alloy (SMA) bars have long been obscured by the lack of an analytical solution, like the analytical solution for duffing equation. The problem results from the nonlinear and hysteretic restoring force of the SMA bar. Here we use a piecewise linear hysteretic model to describe the force-displacement relation of the SMA bar and use the averaging method to solve the equation of motion. We thus obtain an approximate analytical solution of the steady-state response of an SMA mass-spring system. The analytical solution can describe both stable and unstable behaviors of the vibration system and therefore offer a comprehensive understanding of the nonlinear responses. It is shown that the phase transition induced softening nonlinearity bends the frequency response curve (FRC) to the left, while the subsequent rehardening of martensite further bends the FRC to the right, leading to multi-valued regions and jump phenomena. The hysteresis is found to have little influence on the bending but it can significantly suppress the response amplitude. Comparison of the analytical results with experimental data validates the piecewise linear hysteretic model and the analytical solutions. This work provides a theoretical tool for design and vibration control of SMA mass-spring systems.

Keywords: NiTi shape memory alloy, nonlinear vibration, piecewise linear hysteretic model, phase transition, hysteresis, mass-spring system

1. Introduction

Due to the large recoverable deformation and damping capacity, NiTi shape memory alloys (SMAs) have been widely used in medical surgery, smart structures, and civil and seismic engineering [1–5]. Analytical studies of nonlinear dynamics of vibration systems containing SMA components have long been restricted by the complexity of constitutive models of SMAs [6–8]. The complexity results from the nonlinear behavior accompanied by a hysteresis during the forward and reverse phase transitions. Here we use a simple but effective constitutive model and an analytical approach to obtain a full picture of the nonlinear responses of an SMA mass-spring system.

Motivated by industrial demands and academic interests, researchers have so far explored various vibration systems with NiTi SMA components. Based on the constitutive model from Graesser and Cozzarelli [9], Feng and Li [10]

---

*Corresponding author
Email addresses: mzhuo@connect.ust.hk (Mingzhao Zhuo), mzzhuo@gmail.com (Mingzhao Zhuo),
mxiaaa@connect.ust.hk (Minglu Xia), meqpsun@ust.hk (Qingping Sun)

studied the dynamic response of a mechanical system containing an SMA bar and found that phase transition can reduce the resonance frequency and suppress the peak response. Savi and Machado investigated the vibration of a shape memory two-bar truss system [11, 12] using a polynomial constitutive model and presented a general overview [13] of nonlinear dynamics and chaos of smart material systems built with SMAs. Seelecke [14] focused on the response of a rigid mass suspended by a thin-walled SMA tube under isothermal and non-isothermal conditions by numerical simulations. Bernardini, Vestroni, and Lacarbonara [15, 16] numerically studied the thermomechanical responses of a single degree of freedom system with an SMA bar as the spring element using a modified thermomechanical model from Ivshin and Pence [17]. Bernardini and Rega [18] recently proposed a comprehensive thermomechanical modeling framework and compared the performances of different SMA models in terms of the nonlinear dynamic response prediction. Piccirillo et al. studied the primary resonance and free response of an SMA oscillator [19] subjected to harmonic excitation using a polynomial constitutive model and further considered the SMA oscillator [20] under the non-ideal excitation using a thermomechanical model. Lagoudas and Machado [21–23] analyzed the nonlinear dynamics and chaos in a superelastic SMA oscillator using a hysteretic and rate-independent constitutive model under isothermal and non-isothermal conditions by numerical simulation. Moumni et al. [24, 25] employed coupled thermomechanical Zaki-Moumni model [7] to simulate the forced oscillation of an SMA mass-spring-damper system. Xia and Sun [26, 27] investigated the jump phenomena of thermomechanical responses in the frequency, amplitude, and time domains for a torsional system with an NiTi wire and further explored the grain size effect of NiTi polycrystals [28] on the stability of nonlinear dynamic responses. Jose et al. [29] examined an SMA bar as a vibration isolator and evaluated the displacement transmissibility by numerically solving state space equations.

In the vibration systems containing NiTi SMAs, the restoring force is not only nonlinear but also hysteretic because of the hysteresis in the stress strain curve of SMAs during phase transitions. For better utilization of SMA vibration systems, it is important to have a comprehensive understanding of the system responses, including stable and unstable solutions and jump phenomena, and to reveal the effects of nonlinearity and hysteresis (in the restoring force) on the system responses. The numerical studies reported above can accurately simulate the dynamic responses of the vibration systems by using accurate but complicated thermomechanical models [6–8, 17, 23, 30]. However, they have limitations in obtaining the unstable solutions of the nonlinear systems and are not suitable for analyzing the associated jump phenomena. Moreover, numerical studies can only present the overall responses of the system and thus have difficulties in explicitly distinguishing the effects of nonlinearity and hysteresis on the vibration responses. Likewise, experimental studies cannot capture unstable solutions and present the overall responses that are the results of combined effects of nonlinearity and hysteresis. In contrast, analytical solutions can overcome these difficulties to complement numerical and experimental studies.

In this study we present analytical solutions of a mass-spring vibration system (Fig. 1). An SMA bar is applied in the vibration system as the spring element providing the restoring force. Due to martensite phase transitions, the restoring force is nonlinear and hysteretic (Figs. 2 and 3); therefore, the mass-spring system is called a nonlinear and hysteretic vibration system. To consider the nonlinearity and hysteresis, we introduce a piecewise linear hysteretic model (Sec. 2.1) to describe the behavior of NiTi SMAs. The averaging method [31, 32] is then used (Sec. 3) to solve the
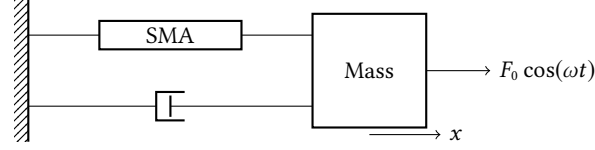
Fig. 1. Illustration of an NiTi SMA mass-spring-damper system.

equation of motion (Sec. 2.2) of the nonlinear and hysteretic system. This analytical approach enables us to quantify the nonlinearity and hysteresis by terms of clear physical meanings (Sec. 3.3). Based on the analytical results, we plot frequency response curves (Sec. 4.1) and phase planes (Sec. 4.2) to demonstrate both stable and unstable solutions and to analyze jump phenomena. Frequency response curves (FRCs) obtained are compared with FRCs by direct numerical integration (Appendix A). Furthermore, we change model parameters (Sec. 4.3) to discuss effects of nonlinearity and hysteresis (the change of nonlinearity and hysteresis can be achieved in experiments by using wires of different grain sizes [33–36]). Finally, we compare the analytical solutions with experimental results of a torsional vibration system (Sec. 5) for the purpose of validation.

2. Nonlinear hysteretic oscillator

The mass-spring mechanical system consists of a mass attached to an NiTi SMA bar and a dashpot as shown in Fig. 1. Here we include the rate-dependent dashpot to make our model general (consider possible viscous components in the vibration system), but our focus is the hysteresis of the NiTi SMA bar that serves as the nonlinear spring element. The restoring force provided by the SMA bar are described by a piecewise linear and hysteretic model in Sec. 2.1. The oscillator is harmonically excited, and the equation of motion is established and nondimensionalized in Sec. 2.2.

2.1. Piecewise linear and hysteretic stress-strain model

Many thermomechanical models [6–8, 17, 23, 30, 37] have been proposed to describe different aspects of the behavior of SMA materials, but they are usually complicated and need numerical methods to obtain the solutions. To quantify the nonlinearity and hysteresis of NiTi SMAs, we use a piecewise linear hysteretic model which can be handled by an approximate analytical method.

For an NiTi bar under uniaxial tension, the stress strain relation can be simplified as a piecewise linear and hysteretic function [38] as shown in Fig. 2. When an external load is applied, the material will first undergo elastic extension in austenite phase until martensite transformation start stress σ_{Ms} is reached. As the stress continues increasing, the forward martensitic phase transition takes place and proceeds until the martensite finish stress σ_{Mf} with generation of a large transformation strain ϵ_L. A further increase of stress leads to the elastic deformation of pure martensite. During unloading, the martensite first deforms elastically until the reverse M→A transition start stress σ_{As}. The reverse phase transition proceeds and finishes at austenite finish stress σ_{Af} with full recovery of the phase transformation strain. Further unloading the austenite brings the strain back to zero. The stress strain curves

3
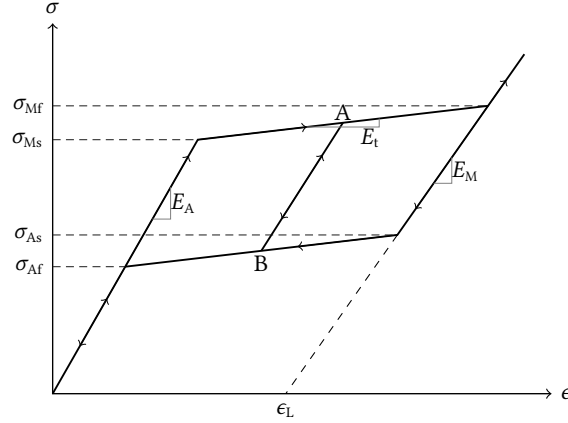
Fig. 2. Stress strain relation of NiTi shape memory alloy in tension. Young's moduli of pure austenite, pure martensite, and their mixture in phase transitions are denoted by E_A, E_M, and E_t, respectively. Martensites start and finish at σ_{Ms} and σ_{Mf}, while austenites start and finish at σ_{As} and σ_{Af}. The maximum transformation strain is denoted by ϵ_L. Line AB represents the linear elastic loading/unloading path of the two-phase mixture in the case of partial phase transitions, and its slope is defined in Eq. (8).

during the elastic deformation of pure martensite and austenites are characterized by their modulus E_M and E_A, respectively. In the forward and reverse phase transitions, the stress strain curves are also approximated to be linear and have the same slopes E_t for simplicity.

Another important issue in modeling is to determine the reloading/unloading path for partial phase transitions. We assume that the volume fraction of martensite ξ scales linearly with the stress in the forward (from σ_{Ms} to σ_{Mf}) and reverse (from σ_{As} to σ_{Af}) phase transitions. Hence, a stress strain point (A) during the forward phase transition corresponds uniquely to a point (B) in the reverse phase transition with the same value of martensite volume fraction ξ. The straight line AB are defined as the linear elastic reloading/unloading path of the two-phase mixture in the case of partial phase transitions (Fig. 2). On this path, no phase transition occurs.

2.2. Equation of motion

The equation of motion for the mechanical vibration system (Fig. 1) is given by

$$m\frac{d^2x}{dt^2} + c\frac{dx}{dt} + F(x) = F_0 \cos(\omega t), \tag{1}$$

where x is the displacement of mass m, c is the viscous damping coefficient, $F(x)$ denotes the nonlinear hysteretic restoring force provided by the NiTi SMA bar, and $F_0 \cos(\omega t)$ represents the external excitation.

To nondimensionalize Eq. (1), we first compute stiffness of the NiTi SMA bar in austenite phase as

$$k_a = \frac{E_A S}{L},$$

where L is the length of the bar, S is the cross-sectional area of the bar. We then let

$$
\begin{aligned}
&\omega_0^2 = \frac{k_a}{m}, \quad \zeta = \frac{c}{2m\omega_0}, \quad \Omega = \frac{\omega}{\omega_0}, \quad \tau = \omega_0 t, \quad y = \frac{x}{x_m} \\
&y' = \frac{dy}{d\tau}, \quad y'' = \frac{d^2y}{d\tau^2}, \quad f(y) = \frac{F(x)}{k_a x_m}, \quad \alpha = \frac{F_0}{k_a x_m},
\end{aligned}
\tag{2}
$$

4

where x_m is the bar extension when martensite phase transition starts. Dividing both sides of Eq. (1) by $k_a x_m$, we arrive at the nondimensionalized form:

$$y'' + 2\zeta y' + f(y) = \alpha \cos(\Omega\tau).$$

By convention, this equation can be rewritten as

$$\ddot{x} + 2\zeta\dot{x} + f(x) = \alpha \cos \omega t. \tag{3}$$

Based on the tensile stress strain curve in Fig. 2, we derive the nondimensionalized force-displacement curve of the SMA bar as shown in Fig. 3. The force-displacement curve includes the compressive part and is made symmetric about the origin for simplicity although the response of an NiTi SMA bar under tension is not exactly the same as under compression [39]. In Fig. 3, the restoring force can be explicitly expressed as follows:

$$f(x) = \begin{cases} kx + (\epsilon + 1 - k)x_I - \epsilon, & \text{I} \\ (\epsilon + 1)x - \epsilon r, & \text{II} \\ x, & \text{III} \\ (\epsilon + 1)x + \epsilon, & \text{IV} \\ kx + (\epsilon + 1 - k)x_V + \epsilon, & \text{V} \\ (\epsilon + 1)x + \epsilon r, & \text{VI} \\ x, & \text{VII} \\ (\epsilon + 1)x - \epsilon, & \text{VIII} \\ (\delta + 1)(x - t), & \text{IX} \\ (\delta + 1)(x + t), & \text{X} \end{cases} \tag{4}$$

All parameters in Eq. (4) and Fig. 3 are defined and explained as follows and will be used in Sec. 4 for discussions. We define ϵ $(-1 \le \epsilon \le 0)$ as

$$\epsilon = \frac{E_t}{E_A} - 1, \tag{5}$$

and δ $(\delta > \epsilon)$ as

$$\delta = \frac{E_M}{E_A} - 1. \tag{6}$$

By definition (5) we see that ϵ characterizes the softening ($E_t < E_A$) nonlinearity during the forward phase transition; Equation (6) indicates that δ represents the rehardening ($E_M > E_t$) nonlinearity after the full forward phase transition. Here r is the ratio of the bar extension at the finish of the reverse phase transition (rx_m) over the bar extension at the start of the forward phase transition (x_m): it characterizes the size of the hysteresis in the vertical direction in Fig. 3; t is associated with the maximum transformation strain ϵ_L (Fig. 2) and defined as

$$t = \frac{L\epsilon_L}{x_m}. \tag{7}$$

5
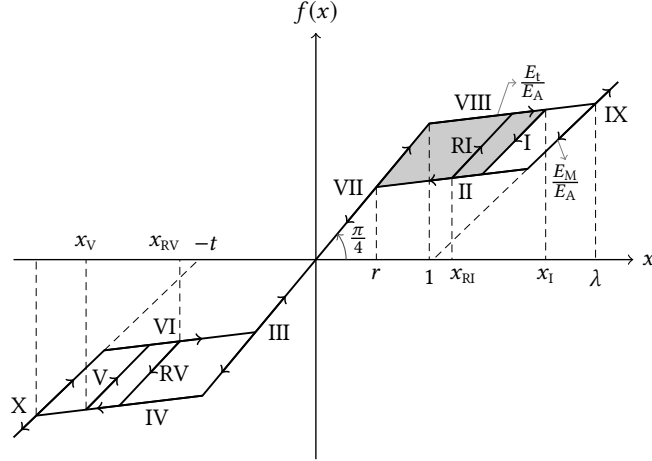
Fig. 3. Piecewise linear hysteretic restoring force $f(x)$ of the NiTi SMA bar as defined in Eq. (4). The filled gray area is the hysteresis loop area H expressed in the second formula of Eq. (11).

The slope k of inner elastic path I and V for partial phase transitions with martensite volume fraction ξ is expressed as

$$k = 1 + \frac{\epsilon \delta \xi}{\epsilon - \delta + \delta \xi}, \tag{8}$$

and the martensite volume fraction ξ is determined by

$$\xi = \begin{cases} \dfrac{x_{\mathrm{I}} - 1}{\lambda - 1}, & \mathrm{I} \\ \dfrac{x_{\mathrm{V}} + 1}{1 - \lambda}, & \mathrm{V} \end{cases} \tag{9}$$

where x_{I} and x_{V} are the values of x at the time when state I and V are entered, and λ is the ratio of the bar extension at the full forward phase transition (λx_{m}) over the bar extension at the start of forward phase transition (x_{m}), which is related to t as

$$\lambda = \frac{\epsilon - (1 + \delta)\, t}{\epsilon - \delta}. \tag{10}$$

The hysteresis loop area H in Fig. 3 depends on the steady-state response amplitude R and is calculated as follows:

$$H = \begin{cases} 0, & R \leq 1 \\ -\epsilon(1-r)\left[2R - 2 - \dfrac{\xi \delta(1-r)}{\epsilon - \delta}\right], & 1 \leq R \leq \lambda \\ -\epsilon(1-r)\left[2\lambda - 2 - \dfrac{\delta(1-r)}{\epsilon - \delta}\right], & R \geq \lambda \end{cases} \tag{11}$$

In the second formula (when $1 \leq R \leq \lambda$), $R = x_{\mathrm{I}}$ and ξ is determined by Eq. (9).

3. Approximate analytical solution

The response of an SMA vibration system generally first experiences a transient state and finally reaches a steady state [26, 27]. The steady-state response is a sinusoidal function of time with the same frequency as the excitation.

Although it is unlikely to have an explicit analytical solution for such a nonlinear hysteretic vibration system, an approximate analytical approach can be used to obtain the steady-state responses and reveal the roles of nonlinearity and hysteresis.

Here the averaging method based on Ref. [31] is employed to solve Eq. (3) by assuming the following form of solution with slowly varying amplitude R and phase angle ϕ

$$\begin{cases} x = R\cos(\omega t + \phi) = R\cos\theta, & (12) \\ \dot{x} = -\omega R\sin(\omega t + \phi) = -\omega R\sin\theta. & (13) \end{cases}$$

This implies

$$\dot{R}\cos\theta - R\dot{\phi}\sin\theta = 0. \tag{14}$$

Differentiating Eq. (13) with respect to time t and then substituting it into Eq. (3), yield

$$-\omega\dot{R}\sin\theta - \omega^2 R\cos\theta - \omega R\dot{\phi}\cos\theta - 2\zeta\omega R\sin\theta + f(R,\theta) = \alpha\cos\omega t. \tag{15}$$

Here considering $x = R\cos\theta$, we use $f(R,\theta)$, instead of $f(x)$ in Eq. (3), to denote the restoring force to explicitly show the dependence on R and θ. Multiplying both sides of Eq. (15) by $\sin\theta$ and $\cos\theta$, and then taking into account Eq. (14), we can get

$$\begin{cases} -\omega\dot{R} - \omega^2 R\sin\theta\cos\theta - 2\zeta\omega R\sin^2\theta + f(R,\theta)\sin\theta = \alpha\cos\omega t\sin\theta, \\ -\omega R\dot{\phi} - \omega^2 R\cos^2\theta - 2\zeta\omega R\sin\theta\cos\theta + f(R,\theta)\cos\theta = \alpha\cos\omega t\cos\theta. \end{cases} \tag{16}$$

Since R and ϕ are assumed to vary slowly compared to θ, Equations (16) can be averaged over one cycle of θ to give

$$\begin{cases} \dot{R} = \dfrac{S(R)}{2\omega} - \dfrac{\alpha\sin\phi}{2\omega} - \zeta R, \\ \dot{\phi} = \dfrac{C(R)}{2R\omega} - \dfrac{\alpha\cos\phi}{2R\omega} - \dfrac{\omega}{2}, \end{cases} \tag{17}$$

where

$$S(R) = \frac{1}{\pi}\int_0^{2\pi} [f(R,\theta)\sin\theta]\,d\theta, \quad C(R) = \frac{1}{\pi}\int_0^{2\pi} [f(R,\theta)\cos\theta]\,d\theta. \tag{18}$$

Due to the piecewise linear restoring force $f(R,\theta)$, $S(R)$ and $C(R)$ are continuous piecewise functions of response amplitude R. Referring to Fig. 3 and Eq. (4), we carefully compute $S(R)$ and $C(R)$ in Eq. (18) and obtain the following expressions for $S(R)$ and $C(R)$:

(1) when $R \leq 1$,

$$S(R) = 0, \quad C(R) = R. \tag{19}$$

(2) when $1 \leq R \leq \lambda$,

$$S(R) = \frac{2}{\pi} \left[\int_0^{\theta_1} f(R, \theta) \sin \theta \, d\theta + \int_{\theta_1}^{\theta_2} f(R, \theta) \sin \theta \, d\theta + \int_{\theta_2}^{\theta_3} f(R, \theta) \sin \theta \, d\theta + \int_{\theta_3}^{\pi} f(R, \theta) \sin \theta \, d\theta \right]$$

$$= \frac{\epsilon(1-r)}{\pi R} \left[2R - 2 - \frac{\xi \delta(1-r)}{\epsilon - \delta} \right],$$

$$C(R) = \frac{2}{\pi} \left[\int_0^{\theta_1} f(R, \theta) \cos \theta \, d\theta + \int_{\theta_1}^{\theta_2} f(R, \theta) \cos \theta \, d\theta + \int_{\theta_2}^{\theta_3} f(R, \theta) \cos \theta \, d\theta + \int_{\theta_3}^{\pi} f(R, \theta) \cos \theta \, d\theta \right] \qquad (20)$$

$$= \frac{\epsilon R}{\pi} (\pi - \theta_1 + \theta_2 - \theta_3) + \frac{\epsilon R}{2\pi} (\sin 2\theta_1 - \sin 2\theta_2 + \sin 2\theta_3) + R$$

$$+ \frac{R}{\pi} (k-1) \left(\theta_1 - \frac{\sin 2\theta_1}{2} \right),$$

where

$$\cos \theta_1 = 1 - \left(1 + \frac{\xi \delta}{\epsilon - \delta} \right) \frac{1-r}{R}, \quad \cos \theta_2 = \frac{r}{R}, \quad \cos \theta_3 = -\frac{1}{R},$$

$$k = 1 + \frac{\epsilon \delta \xi}{\epsilon - \delta + \delta \xi}, \quad \xi = \frac{R-1}{\lambda - 1}, \quad \lambda = \frac{\epsilon - (1+\delta)t}{\epsilon - \delta},$$

and $R \cos \theta_1$, $R \cos \theta_2$, $R \cos \theta_3$ are the values of x at the intersection points between I and II, II and III, III and IV, respectively.

(3) when $R \geq \lambda$,

$$S(R) = \frac{\epsilon(1-r)}{\pi R} \left[2\lambda - 2 - \frac{\delta(1-r)}{\epsilon - \delta} \right],$$

$$C(R) = \frac{\epsilon R}{2\pi} (\sin 2\theta_1 - \sin 2\theta_2 + \sin 2\theta_3 - \sin 2\theta_4) - \frac{\epsilon R}{\pi} (\theta_1 - \theta_2 + \theta_3 - \theta_4) + R \qquad (21)$$

$$- \frac{\delta R}{2\pi} (\sin 2\theta_1 - \sin 2\theta_4 - 2\theta_1 + 2\theta_4) + \delta R,$$

where

$$\cos \theta_1 = \left[\lambda - \frac{\epsilon(1-r)}{\epsilon - \delta} \right] \frac{1}{R}, \quad \cos \theta_2 = \frac{r}{R}, \quad \cos \theta_3 = -\frac{1}{R}, \quad \cos \theta_4 = -\frac{\lambda}{R},$$

and $R \cos \theta_1$, $R \cos \theta_2$, $R \cos \theta_3$, $R \cos \theta_4$ are the values of x at the intersection points between IX and II, II and III, III and IV, IV and X, respectively.

3.1. Steady-state response

In the steady state, letting $\dot{R} = \dot{\phi} = 0$ in Eq. (17) gives

$$\begin{cases} -2\zeta \omega R_s + S(R_s) = \alpha \sin \phi_s, \\ -\omega^2 R_s + C(R_s) = \alpha \cos \phi_s, \end{cases} \qquad (22)$$

where the subscript "s" denotes the steady state. From Eq. (22), FRCs of amplitude and phase can be obtained via

$$[S(R_s) - 2\zeta \omega R_s]^2 + [C(R_s) - \omega^2 R_s]^2 = \alpha^2 \qquad (23)$$

and

$$\tan \phi_s = \frac{S(R_s) - 2\zeta \omega R_s}{C(R_s) - \omega^2 R_s}, \qquad (24)$$

where $\phi_s \in [-\pi, 0]$. Expanding Eq. (23) gives

$$\omega^4 + a\omega^2 + b\omega + c = 0, \tag{25}$$

where

$$a = \left[4\zeta^2 - 2\frac{C(R_s)}{R_s}\right], \ b = -4\zeta\frac{S(R_s)}{R_s}, \ c = \left[\frac{S(R_s)}{R_s}\right]^2 + \left[\frac{C(R_s)}{R_s}\right]^2 - \frac{\alpha^2}{R_s^2}.$$

Equation (25) is used to obtain the FRC, which describes the steady-state response amplitude R_s as a function of the excitation frequency ω at a given excitation amplitude α. Specifically, FRCs are obtained by solving Eq. (25) for the excitation frequency ω in terms of the response amplitude R_s, instead of calculating R_s from ω. At a given response amplitude R_s, there are four roots ω for the quartic polynomial equation (25), but only two of them are positive and used to plot the FRC. The formulas for roots of Eq. (25) can be found in mathematical handbooks [40] and is not presented here for the sake of conciseness.

The last step is to determine the maximum response amplitude where only one positive root exists. The necessary conditions for the maximum response amplitude are

$$\begin{cases} \omega_c^4 + a\omega_c^2 + b\omega_c + c = 0, \\ 4\omega_c^3 + 2a\omega_c + b = 0, \end{cases} \tag{26}$$

where ω_c is the critical frequency at which the maximum response amplitude occurs. After elimination of ω_c, the following expression is obtained

$$\left[2a\left(4c - a^2\right) - 9b^2\right]\left[8c\left(4c - a^2\right) + 3ab^2\right] + 2b^2\left(a^2 + 12c\right)^2 = 0, \tag{27}$$

which can be solved for the maximum response amplitude.

For the special case of zero viscous damping ($\zeta = 0$, so $b = 0$), the FRC expression is more concise:

$$\omega^2 = \frac{C(R_s) \pm \sqrt{\alpha^2 - [S(R_s)]^2}}{R_s}. \tag{28}$$

Here we can get the two positive square roots for each response amplitude R_s. Note that, in this particular case, hysteresis of the NiTi bar still exists and is considered in $S(R_s)$. The maximum response amplitude occurs at the point where ω^2 has a double root: $\alpha^2 = [S(R_s)]^2$. According to Eq. (28), we can also define the backbone curve that quantifies the bend of FRCs as

$$\omega = \sqrt{\frac{C(R_s)}{R_s}}. \tag{29}$$

3.2. Stability analysis

Actually, more than one solution exists at some excitation frequencies, but not all of them are stable. To determine whether a solution is stable, the Jacobian matrix of Eqs. (17) at (R_s, ϕ_s) is first computed as

$$\begin{aligned} J &= \frac{1}{2\omega}\begin{bmatrix} \frac{dS}{dR} - 2\zeta\omega & -\alpha\cos\phi \\ \frac{\partial}{\partial R}\left(\frac{C - \alpha\cos\phi}{R}\right) & \frac{\alpha\sin\phi}{R} \end{bmatrix}_{(R_s, \phi_s)} \\ &= \frac{1}{2\omega}\begin{bmatrix} \frac{dS}{dR} - 2\zeta\omega & R\omega^2 - C \\ \frac{1}{R}\left(\frac{dC}{R} - \omega^2\right) & \frac{S}{R} - 2\zeta\omega \end{bmatrix}_{R=R_s}. \end{aligned} \tag{30}$$

The trace of the Jacobian matrix (30) is found to be always negative:

$$T = \left[\frac{1}{2R\omega} \frac{d(RS)}{dR} - 2\zeta \right]_{R=R_s} = - \left[\frac{1}{2R\pi\omega} \frac{dH}{dR} + 2\zeta \right]_{R=R_s} < 0.$$

This is because the hysteresis loop area H increases with R monotonically, which can be verified in Fig. 3 and Eq. (11). The determinant of Jacobian matrix (30) is

$$D = \frac{1}{4\omega^2} \left[\left(\frac{dS}{dR} - 2\zeta\omega \right) \left(\frac{S}{R} - 2\zeta\omega \right) + \left(\frac{dC}{dR} - \omega^2 \right) \left(\frac{C}{R} - \omega^2 \right) \right]_{R=R_s} \tag{31}$$

$$= \frac{1}{8\omega^2 R_s} \left[\frac{dW(R)}{dR} \right]_{R=R_s}, \tag{32}$$

where

$$W(R) = [S(R) - 2\zeta\omega R]^2 + \left[C(R) - \omega^2 R \right]^2 - \alpha^2. \tag{33}$$

By the trace-determinant criterion [41], the steady-state solution will be stable if $D > 0$ but unstable if $D < 0$ when $T < 0$.

3.3. Physical interpretation

To understand the physical meaning of $S(R)$ and $C(R)$, the restoring force $f(x)$ in Eq. (3) is approximated by Fourier series with the primary harmonic:

$$f(x) = f(R\cos\theta) \approx f_0 + S\sin\theta + C\cos\theta, \tag{34}$$

where f_0 is calculated to be zero in the current model

$$f_0 = \frac{1}{2\pi} \int_0^{2\pi} f(R, \theta)\, d\theta = 0$$

and coefficients of the primary harmonic—S and C—have the same expressions as in Eq. (18). Expressing $\sin\theta$ and $\cos\theta$ in Eq. (34) by x and $\dot{x}$ according to Eqs. (12) and (13), we can reformulate the restoring force as

$$f(x) = -\frac{S(R)}{\omega R}\dot{x} + \frac{C(R)}{R}x. \tag{35}$$

Substituting Eq. (35) into the governing equation (3), we obtain the equivalent equation of motion

$$\ddot{x} + \left(2\zeta - \frac{S(R)}{\omega R} \right)\dot{x} + \frac{C(R)}{R}x = \alpha\cos\omega t. \tag{36}$$

We can also arrive at the steady-state solution (22) by solving Eq. (36) with a standard method, which can be found in textbook [42].

As Eq. (35) indicates, the hysteretic nonlinear restoring force $f(x)$ can be approximated as the sum of a rate-independent (because ω in the denominator cancels out the rate effect of $\dot{x}$) damping term (the first term) and a nonlinear force term (the second term). In the bracket of Eq. (36), the first term represents the rate-dependent viscous damping of the vibration system, while the second term comes from the hysteresis of SMAs. In the steady state, the energy dissipated per cycle by the second term is calculated to be exactly the same as the hysteresis loop area in Eq. (11):

$$W_d = \pi \left(-\frac{S(R)}{\omega R} \right) \omega R^2 = -\pi RS = H, \tag{37}$$
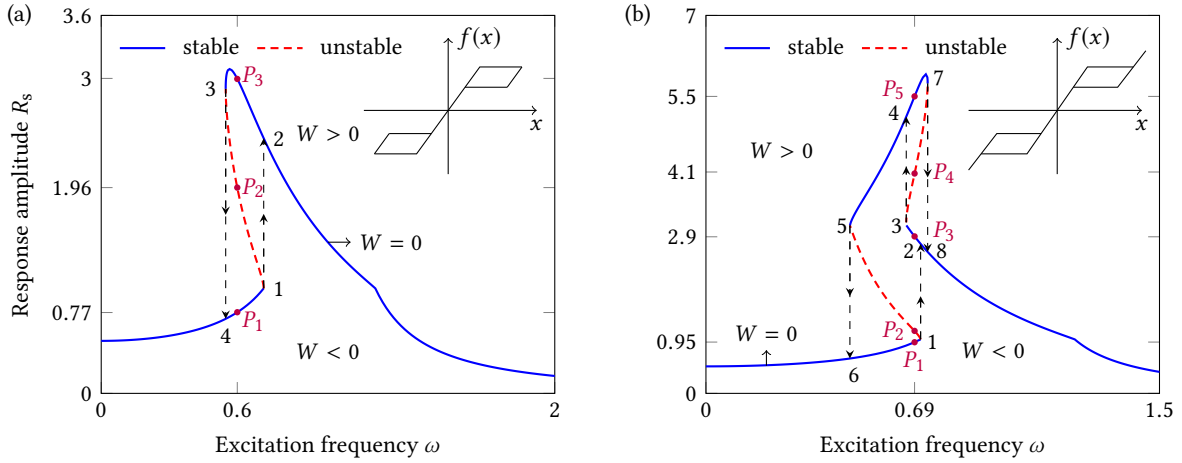
Fig. 4. Frequency response curves (FRCs) showing a single bend in (a) and double bends in (b). The system parameters are $\epsilon = -1.0$, $\zeta = 0.08$, $r = 0.5$, $\alpha = 0.5$ for (a) and $\epsilon = -1.0$, $\delta = -0.1$, $\zeta = 0.045$, $r = 0.5$, $t = 2.0$, $\alpha = 0.5$ for (b). W is defined in Eq. (33), P_1 to P_5 are stable and unstable solutions corresponding to Fig. 6. The inset diagrams show the force-displacement curves to obtain the FRCs.

where S is expressed in Eqs. (19), (20), and (21). The calculation in Eq. (37) can be found in equation (3.7.2) of textbook [42]. This equivalence validates the average method in terms of energy dissipation. It is remarked that the nonlinear force term is mainly determined by the nonlinearity and depends weakly on the hysteresis.

4. Results and discussions

This section shows frequency response curves (FRCs) from the approximate analytical solution and discusses the effects of nonlinearity and hysteresis. Two typical FRCs are presented to show the multi-valued region and jump phenomena, and then the analytical solution is compared with results by numerical method for a cluster of FRCs. The phase planes clearly show the stability of analytical solutions in multi-valued regions of the FRCs. Finally, the effects of nonlinearity and hysteresis are investigated by comparing FRCs at different model parameters.

4.1. Frequency response curves

Figure 4 shows two typical FRCs: one has a single bend while the other has double bends. The FRC in Fig. 4a bends to the left resulting in a multi-valued region. The bending to the left is caused by material softening due to martensitic phase transition. In this case, the maximum deformation is in the partial phase transition region, i.e., the maximum response amplitude does not exceed the full phase transition threshold ($R_s < \lambda$). The FRC in Fig. 4b first shows a bending to the left and then a subsequent bending to the right leading to an "S" shape with two overlapped multi-valued regions in the frequency domain. The first bending to the left is due to martensitic phase transition, while the subsequent bending to the right is attributed to the elastic deformation of martensite phase after the full phase transition.

In Fig. 4, the solid curves denote the stable solutions, which can be realized in experiments and numerical simulations [24, 27]; however, those unstable solutions represented by the dashed lines can not be realized in actual responses
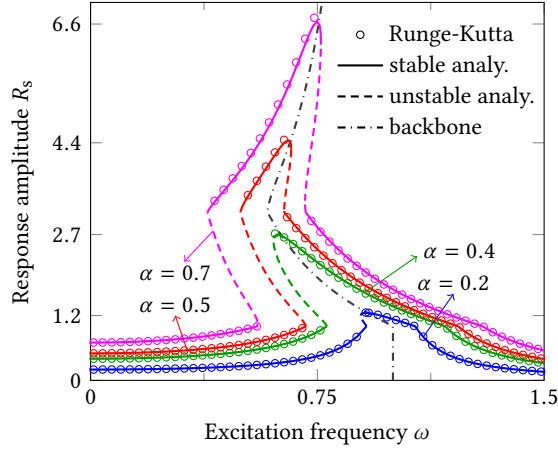
Fig. 5. Frequency response curves at different excitation amplitudes. The system parameters are $\epsilon = -1.0$, $\delta = -0.1$, $\zeta = 0.06$, $r = 0.5$, $t = 2.0$.

no matter how the excitation frequency is exerted. To identify the unstable solutions, the determinant D (defined in Eq.(32)) on the dashed line is evaluated according to the trace-determinant criterion (Sec. 3.2). Specifically, we check the value of W defined in Eq. (33). It is obvious that W is equal to zero ($W = 0$) on the FRC because Eq. (23) exactly corresponds to $W = 0$. Below the FRC, $W < 0$, and above the FRC, $W > 0$. Therefore, we can conclude $D \propto \partial W / \partial R_s \approx \Delta W / \Delta R_s < 0$ on the dashed line and the solution is unstable. We also calculate the specific value of D according to its definition (31) and further confirm that the determinant D on the dashed line is negative.

Jump phenomena are observed in the multi-valued regions. In Fig. 4a, the response amplitude jumps up from point 1 to 2 and then decreases as the excitation frequency increases quasi-statically (compared to the variation of the excitation and response). With decreasing excitation frequency, the response amplitude jumps down from point 3 to 4 and then decreases. However, the double bends in Fig. 4b make the path dependence of the jump phenomena more complex. With increasing excitation frequencies, the response amplitude jumps up from 1 to 2 and then decreases continuously. If the frequency is reduced after point 2, the response amplitude will first increase and then jump up from 3 to 4. Afterwards, the response amplitude either decreases and jumps down from 5 to 6 or increases and jumps down from 7 to 8 depending on the variation of the excitation frequency.

Figure 5 shows a family of FRCs at different excitation amplitudes. The good agreement between analytical solutions and numerical results by Runge-Kutta method (Appendix A) suggests that the assumption of primary resonance in the response is reasonable and that the analytical method is appropriate for the considered vibration system. The absence of numerical results on the dashed lines further confirms that unstable solutions can not be realized in direct numerical simulations. The backbone curve defined in Eq. (29) exhibits an "S" shape that differs significantly from a vertical line at the natural frequency for a linear vibration system.
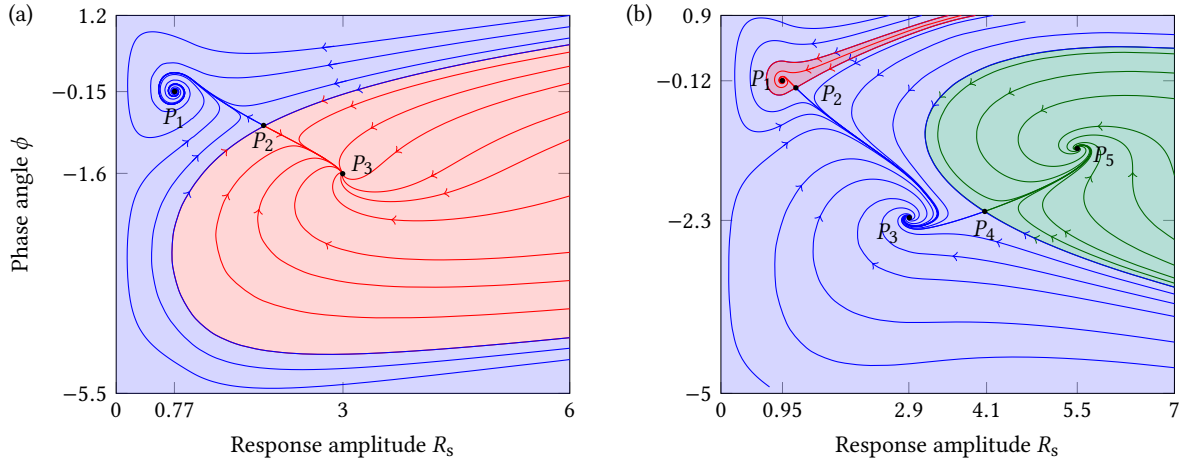
Fig. 6. Phase planes showing three (a) and five (b) steady-state solutions. The system parameters are $\epsilon = -1.0$, $\zeta = 0.08$, $r = 0.5$, $\alpha = 0.5$, $\omega = 0.6$ for (a) and $\epsilon = -1.0$, $\delta = -0.1$, $\zeta = 0.045$, $r = 0.5$, $t = 2.0$, $\alpha = 0.5$, $\omega = 0.69$ for (b).

4.2. Phase plane

In nonlinear vibration systems, initial conditions (e.g., initial position and velocity of the mass block in Fig. 1) determine which steady-state solution is finally realized when multi-valued responses exist [43]. The following forward time difference scheme is derived from Eq. (17) to calculate trajectories starting at different initial points in the phase plane:

$$\begin{cases} \dfrac{R_{n+1} - R_n}{\Delta t} = \dfrac{S(R_n)}{2\omega} - \dfrac{A}{2\omega} \sin\phi_n - \zeta R_n, \\ \dfrac{\phi_{n+1} - \phi_n}{\Delta t} = \dfrac{C(R_n)}{2R_n\omega} - \dfrac{A}{2R_n\omega} \cos\phi_n - \dfrac{\omega}{2}. \end{cases} \tag{38}$$

Corresponding to the three solutions at a specific frequency in Fig. 4a, the phase plane in Fig. 6a shows two stable spirals (P_1 and P_3) and one unstable saddle P_2. All initial conditions in the red area lead to the stable spiral P_3 corresponding to the steady-state solution on the upper branch in Fig. 4a, while all initial conditions in the blue area arrive at the stable spiral P_1 corresponding to the steady-state solution on the lower branch in Fig. 4a. The saddle point P_2 corresponds to the unstable solution marked on the dashed line in Fig. 4a.

The phase plane in Fig. 6b shows the five steady-state solutions in the overlapped multi-valued region of Fig. 4b. Points P_1, P_3 and P_5 are three stable spirals; P_2 and P_4 are two unstable saddles. They correspond to the five solutions denoted by solid dots in Fig. 4b respectively. The three stable spirals have their respective domains of attraction shaded by three different colors. If the frequency is increased beyond the five-solution region, P_1 and P_2 will disappear and the attraction domain of P_1 will be merged into P_3, degenerating into the three-solution case. On further increases of the excitation frequency, P_4 and P_5 will also disappear leading to only one solution. Reversely, if the frequency decreases continuously, P_3 and P_4 will disappear first and the attraction domain of P_3 will turn into that of P_5. Finally, P_2 and P_5 will also vanish with only one steady-state solution remaining.
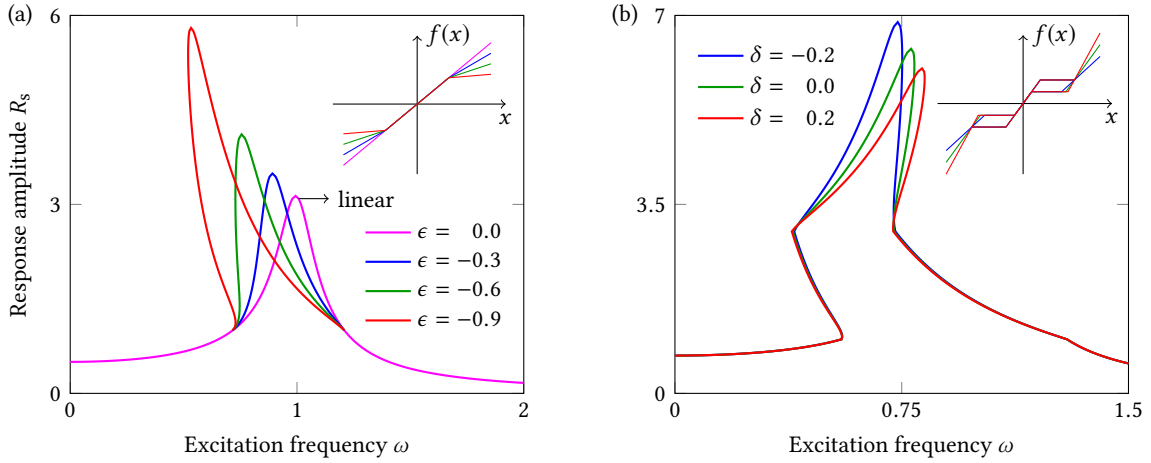
Fig. 7. Effects of nonlinearity on frequency response curves in the softening (a) and rehardening (b) region. The system parameters are $\zeta = 0.08$, $r = 1.0$, $\alpha = 0.5$ for (a) and $\epsilon = -1.0$, $\zeta = 0.06$, $r = 0.5$, $\lambda = 3.0$, $\alpha = 0.7$ for (b).

4.3. Effects of nonlinearity and hysteresis

The softening nonlinearity is characterized by ϵ (ranging from -1 to 0) in Eq. (5). When $\epsilon = 0$ there is no phase transition and therefore no nonlinearity; when $\epsilon = -1$ the phase transition occurs on the stress plateau and the softening nonlinearity is maximum in our model. As ϵ decreases from 0 to -1, modulus E_t decreases from E_A to 0 and the softening nonlinearity increases. In Fig. 7a, the FRC gradually bends to the left with the increase of softening nonlinearity, and the reduction of E_t also results in the increase of the maximum response amplitude. Here to focus on the effect of softening nonlinearity, the transformation strain ϵ_L (or λ in Eq. (10)) is set to be large enough to ensure all the responses are within the phase transition region and the hysteresis is removed by letting $r = 1$ according to Eq. (11). Therefore, bending of the FRC to the left and the increased maximum amplitude are solely caused by softening of modulus E_t.

The rehardening nonlinearity after the full martensite phase transition is characterized by δ ($\delta > \epsilon$) in Eq. (6). Figure 7b shows that, when the deformation enters the rehardening region, the FRC bends to the right and the bending increases with the hardening ($\delta = -0.2$ to $\delta = 0.2$) for a given softening nonlinearity $\epsilon = -1.0$. Furthermore, for a given ϵ the larger the rehardening nonlinearity δ, the smaller the maximum response amplitude, which indicates the suppressing of response amplitude by the rehardening nonlinearity.

We now examine the effect of hysteresis H that depends on two parameters—r and ϵ. From Eq. (11), the hysteresis loop area H increases as r decreases from 1 to 0 at a fixed value of ϵ (< 0). Figure 8a shows the FRCs in the phase transition region (no rehardening) at different values of r, while Fig. 8b shows the FRCs with the rehardening nonlinearity beyond the full martensite phase transition. It is seen that the response amplitudes in both cases decrease with the increase of hysteresis. Therefore, the effect of hysteresis is mainly to suppress the vibration response amplitude without affecting the bend of FRCs. It is remarked that the hysteresis H discussed above is solely from SMAs and here we do not consider the effect of viscous damping by using a fixed coefficient ζ.

14
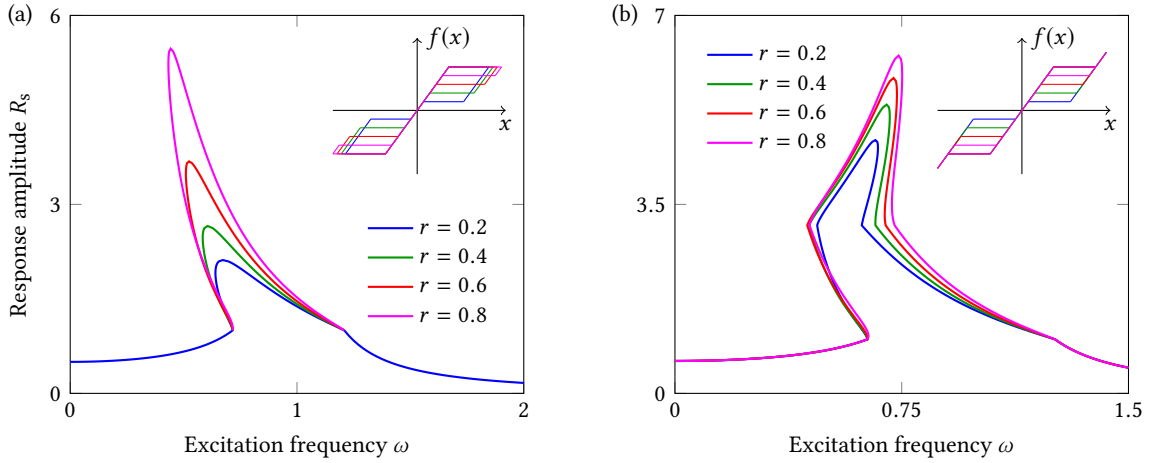
Fig. 8. Effect of hysteresis on frequency response curves by varying r at a fixed ϵ. The system parameters are $\epsilon = -1.0$, $\zeta = 0.08$, $\alpha = 0.5$ for (a) and $\epsilon = -1.0$, $\zeta = 0.06$, $\delta = -0.1$, $t = 2.0$, $\alpha = 0.7$ for (b).

Now we change the hysteresis by varying ϵ at a fixed value of r. The hysteresis H (Eq. (11)) increases as ϵ decreases from 0 to -1 at a fixed value of r (< 1). In contrast to the increasing response amplitude in Fig. 7a, the maximum response amplitude decreases with decreasing ϵ (increasing softening nonlinearity) as shown in Fig. 9. This indicates that the suppressing effect of hysteresis on the response amplitude can even outweigh the enhancing effect of softening nonlinearity. However, the bending of FRCs in Fig. 9 has the same trend as in Fig. 7a, confirming that the bend of FRC is mainly determined by the nonlinearity but almost independent of the hysteresis.

5. Comparison with experimental data

To validate our model and analytical solutions, we simulate the experiments in Refs. [27, 28] where a SMA torsional vibration system was built and the vibration responses were measured. The SMA wires used are of different grain sizes (in average) and their torsional behaviors are consequently different (Fig. 6a in Ref. [28]); different torsional behaviors impact the responses of the vibration system (Fig. 7 in Ref. [28]). The torsional behavior can be described by the piecewise linear hysteretic model, and therefore the analytical method can be used to predict the vibration responses.

In the experimental setup, excitation was not directly applied to the mass block but to the SMA bar (see Fig. 3 of Ref. [27] and Fig. 1 of Ref. [28]). After manipulating the equilibrium equation we obtain the following equivalent equation of motion (similar to Eq. (1) in Ref. [27]):

$$J\ddot{\gamma} + c\dot{\gamma} + M_s(\gamma) = (2\pi f)^2 AJ \sin(2\pi f t), \tag{39}$$

where γ is the rotation angle of the NiTi SMA wire, J is the rotational moment of inertia, c is the viscous damping coefficient, M_s is the restoring torque by the NiTi SMA wire, and $(2\pi f)^2 AJ \sin(2\pi f t)$ is the equivalent external excitation. The torsional vibration system does not contain any viscous damping component; therefore, we only
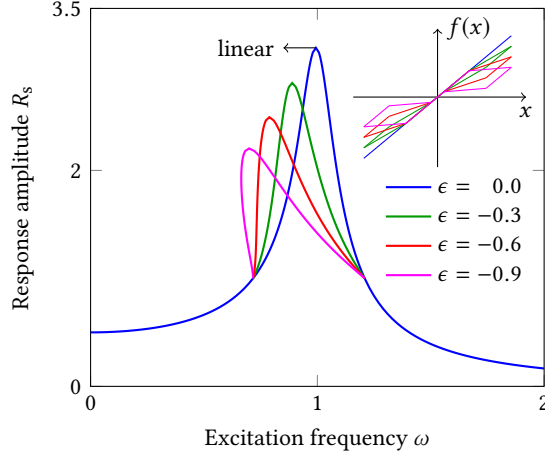
Fig. 9. Effect of hysteresis on frequency response curves by changing ϵ at a small r. The system parameters are $\zeta = 0.08$, $r = 0.2$, $\alpha = 0.5$.

consider the hysteresis (included in M_s) between forward and reverse phase transitions and set the viscous damping coefficient to be zero (i.e., $c = 0$).

To make the force term M_s more clear, we explicitly express its torsional part (the inverse torsional part is symmetric, referring to Eq. (4) and Fig. 3) as

$$
M_s = \begin{cases}
k_a\gamma + (k_t - k_a)(x_I - \gamma_m), & \text{I} \\
k_t\gamma + (k_a - k_t)r\gamma_m, & \text{II} \\
k_a\gamma, & \text{VII} \\
k_t\gamma + (k_a - k_t)\gamma_m, & \text{VIII.}
\end{cases}
\tag{40}
$$

In these expressions, the restoring torque M_s is not nondimensionalized and only takes the transformation softening stage into account. The subsequent rehardening part is disregarded because the maximum rotation in experiments are within the softening region as shown in Figs. 10 and 12. The four parameters to be determined here are stiffness of austenite k_a, stiffness of the phase transition k_t, the wire rotation γ_m when martensite phase transition starts, and r that characterizes the size of hysteresis (Fig. 3).

The piecewise linear hysteretic model is first adjusted to fit the torque-rotation angle curve of the SMA wire to obtain the four material parameters (k_a, k_t, γ_m, r) for M_s in Eq. (40), and the equation of motion (39) is then solved with the method in Sec. 3. The rotational moment of inertia J of the mass block and excitation amplitude A and frequency f can be found in Refs [27, 28]. In plots of FRCs (Fig. 11 and 13), the steady-state response amplitude (on the y axis) by our analytical method is doubled because experiments measured the steady-state peak-to-valley magnitude which is twice the response amplitude as we define in Eq. (12).

Figures 10 and 11 show the experimental data from Figs. 4 and 6 of Ref. [27], respectively, and the results of our analytical approach. It is demonstrated in Fig. 10 that the piecewise linear hysteretic model can well describe the torque-rotation angle response of the SMA wire. Figure 11 shows analytical and experimental FRCs at four excitation
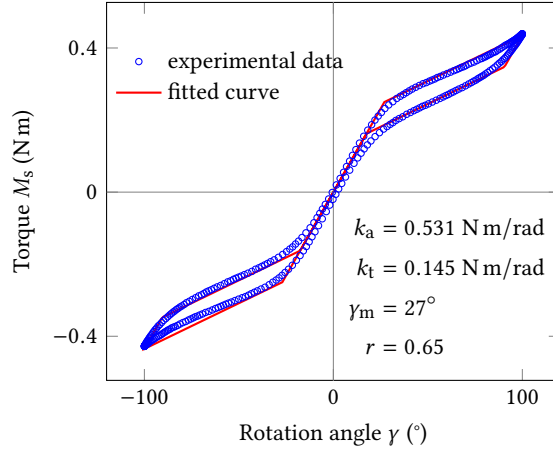
Fig. 10. Torque-rotation angle relation of the NiTi wire. Experimental data are from Ref. [27].

amplitudes $A = 3°, 6°, 9°, 12°$. The rotational moment of inertia is $J = 0.032$ kg m^2. For each excitation amplitude, independent experiments are performed at discrete frequencies in the ascending order (from 0.4 Hz up to 0.7 Hz at an interval of 0.005 Hz) and descending order (from 0.7 Hz down to 0.4 Hz at 0.005 Hz interval). The analytical FRCs show the frequency span from 0.4 to 0.8 Hz. As we can see, the experimental data points are basically located around the analytical FRCs and the analytical solutions are able to capture the trend of FRC bending due to material softening. In the left lower part of the FRCs, the response amplitude is small and the SMA wire behaves linearly; the analytical solution here is actually that of a linear vibration system. The right upper part with larger response amplitude has already entered the softening part of the SMA torsional wire.

Figs. 12 and 13 show experimental data in Ref. [28] for torsional behaviors and FRCs of SMA wires of different grain sizes. In experiments for all grain sizes, the excitation amplitude was fixed at $A = 5°$ and the excitation frequency f varied in the range of 0.4 and 0.8 Hz according to the ascending and descending order with an interval of 0.01 Hz. The system has a rotational moment of inertia of $J = 0.01875$ kg m^2. At the small grain size of 10 nm, the torque-rotation angle relation is almost linear with a quite small hysteresis; the response is therefore similar to that of a linear vibration system: the FRC shows a peak without bending. As the grain size increases, the torque-rotation angle curve shows a more and more clear softening part with increased hysteresis, and correspondingly the FRC bends more and more to the left. As we can see, the piecewise linear hysteretic model can capture the variation of the stiffness and hysteresis of the torque-rotation angle relations (Fig. 12), and the analytical solutions can basically predict the FRCs (Fig. 13). The model and analytical solution can thus be further used to study grain size effect on responses of SMA vibration systems.

It is remarked that the experimental data points only cover part of the FRCs in Figs. 11 and 13: the multi-valued region is not clearly observed in experimental FRCs. In this sense, the analytical method is important for us to quickly detect all the stable and unstable solutions and show a full picture of the solution, which can in turn provide practical guidelines for experimental design of SMA vibration systems.
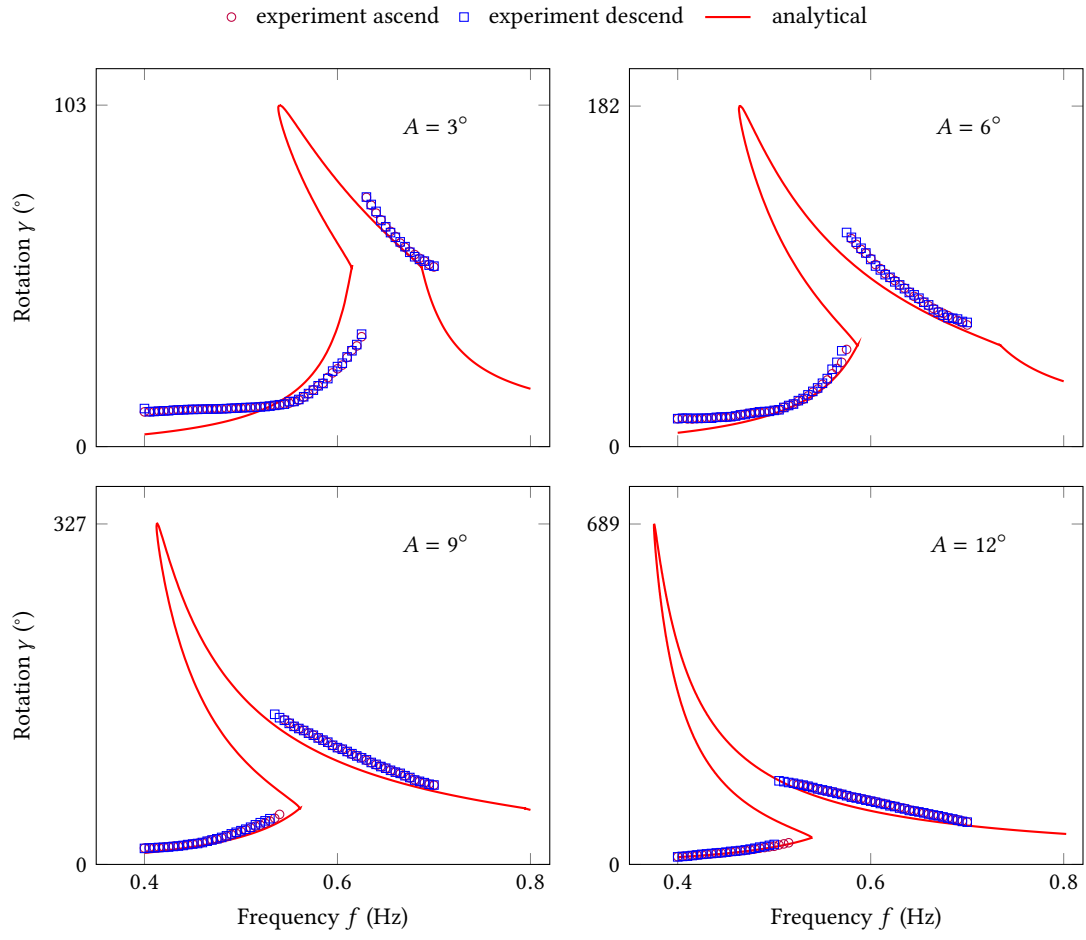
Fig. 11. Frequency response curves at four different excitation amplitudes A. Experimental data are from Ref. [27]. In the legend "ascend" and "descend" refer to changing the excitation frequency in ascending and descending order, respectively.
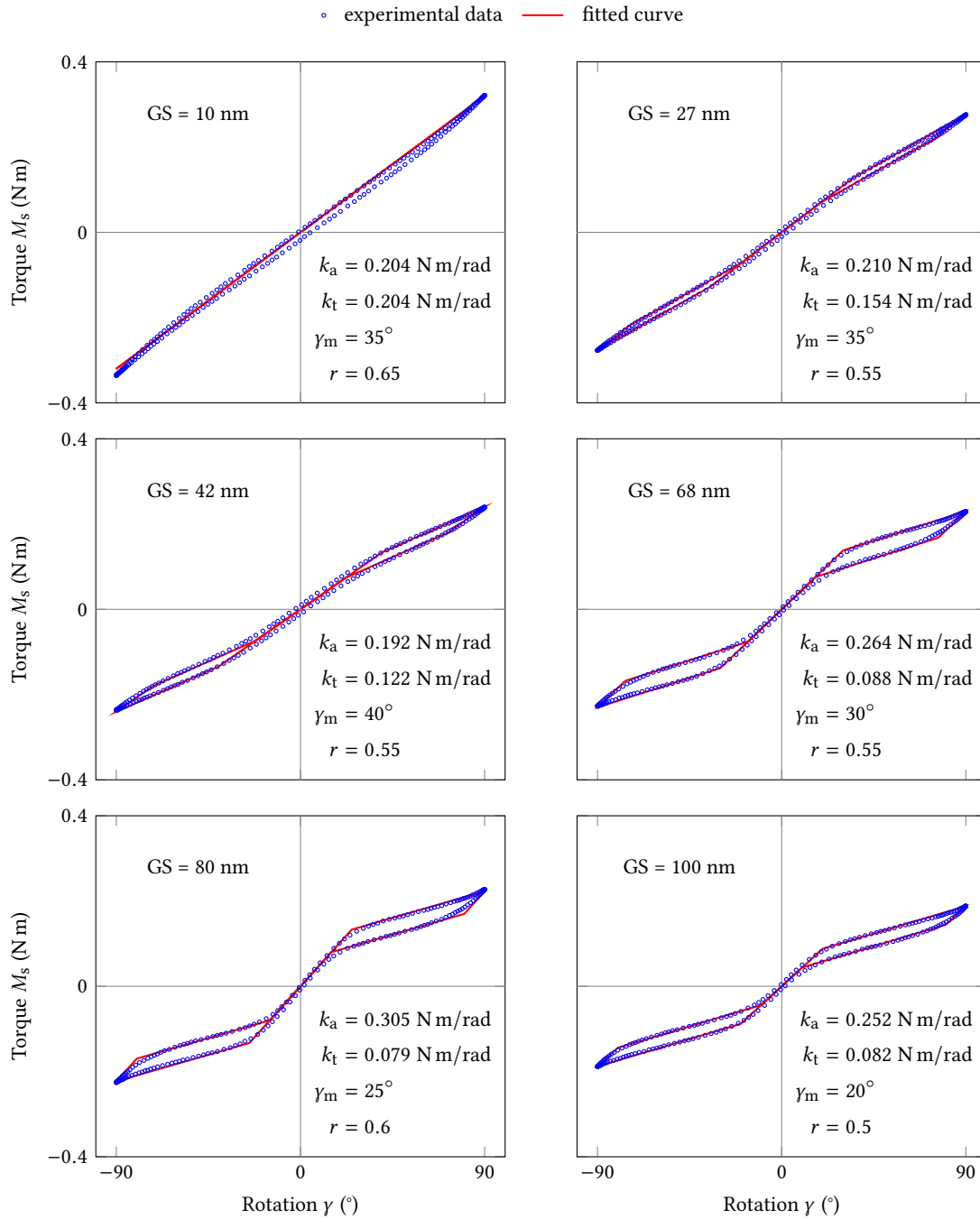
Fig. 12. Torque-rotation angle curves of NiTi SMA wires of different average grain sizes (GS). Experimental data are from Ref. [28].
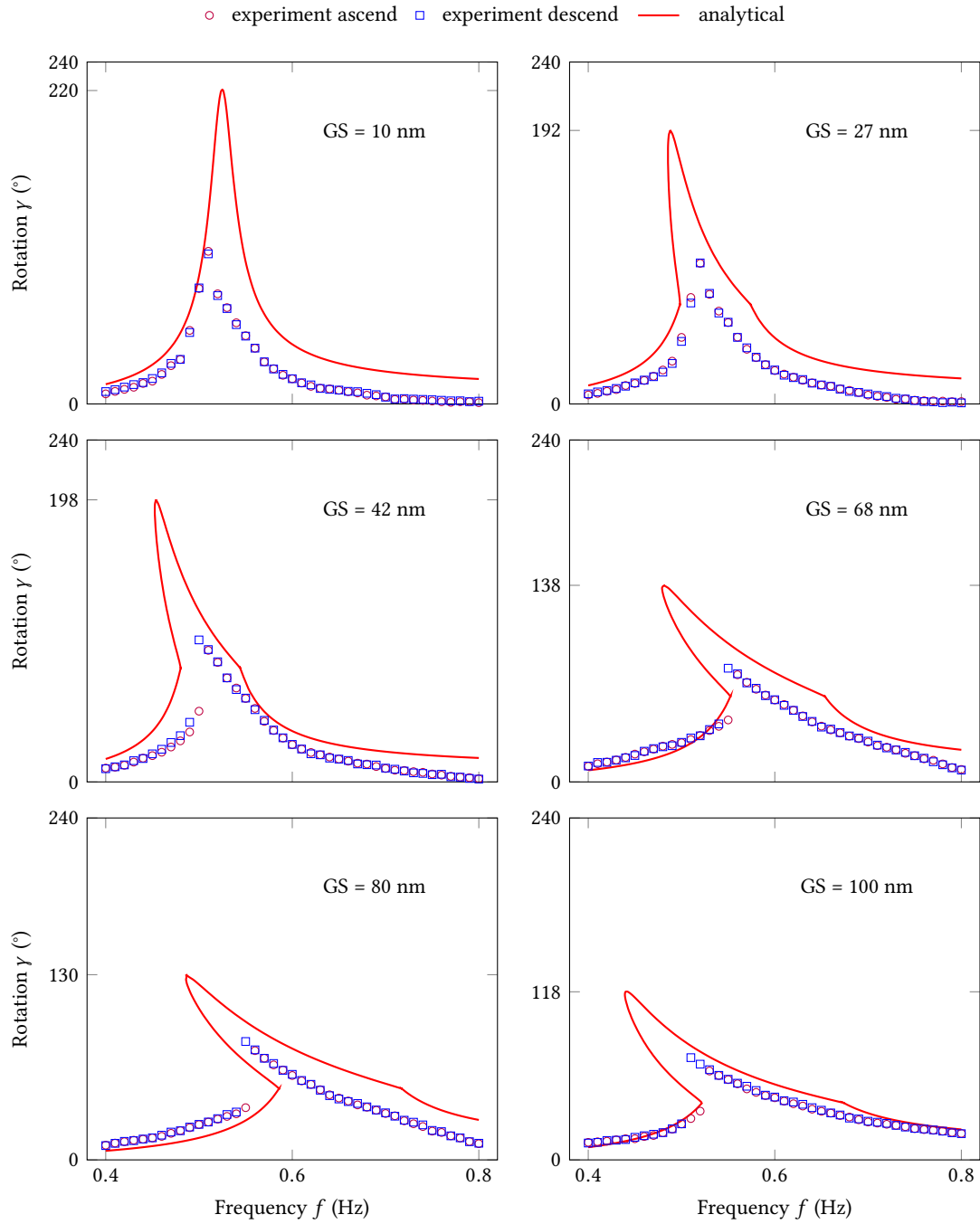
Fig. 13. Frequency response curves of NiTi SMA wires of different average grain sizes (GS) at excitation amplitude of $A = 5°$. Experimental FRCs are from Ref. [28]. In the legend "ascend" and "descend" refer to changing the excitation frequency in ascending and descending order, respectively.

6. Conclusions

A piecewise linear hysteretic model is used to describe the constitutive behavior of an SMA bar, and this simple but effective model enables us to examine an SMA mass-spring system using an approximate analytical method. The analytical method captures all the stable and unstable solutions and analyzes the jump phenomena, which can facilitate the understanding of experimental and numerical simulation results. We show that the nonlinear hysteretic restoring force of an SMA bar can be decomposed into a nonlinear force term and a hysteresis term (Eq. (35)). The effects of nonlinearity and hysteresis on FRCs are revealed by the parametric study: softening nonlinearity by the phase transition bends the FRC to the left, while subsequent rehardening of martensite bends it to the right, leading to an S-shaped FRC; hysteresis can significantly suppress the vibration by energy dissipation, but almost does not affect the bend of FRCs.

The piecewise linear hysteretic model and proposed analytical method are validated by comparison with experimental results of a torsional vibration system. Our analytical solutions can provide guidelines for design of vibration systems to achieve desired performance. The model and analytical method also apply to mechanical systems containing nanostructured NiTi SMAs to study the grain size effect on vibration responses.

Acknowledgments

Appendix A. Numerical integration

To compare with the analytical solution, we also develop direct numerical integration procedures. Equation (3) is a second order ordinary differential equation, and it can be readily solved in each state by an explicit finite difference technique such as the fourth order Runge-Kutta method that is used in our computation (Fig. 5). The major difficulty lies in the transition between those different states. According to the definition of each state in Eq. (4) and Fig. 3, the rules for all state transitions are given in Table A.1, and the key point is to check whether a state transition occurs at each time step based on these rules.

In the numerical calculation, one more issue to be addressed is to describe the reloading paths in the cases of partial reverse phase transitions; hence, two more states (Fig. 3) are added:

$$f(x) = \begin{cases} kx + (\epsilon + 1 - k)x_{\mathrm{RI}} - \epsilon r, & \mathrm{RI} \\ kx + (\epsilon + 1 - k)x_{\mathrm{RV}} + \epsilon r, & \mathrm{RV} \end{cases}$$

where the slope of the inner path is determined by

$$k = 1 + \frac{\epsilon \delta \xi}{\epsilon - \delta + \delta \xi},$$

Table A.1. Rules for state transitions.

Transition	Conditions		Transition	Conditions	
IX → II	$x = \lambda - \frac{\epsilon(1-r)}{\epsilon-\delta}$,	$\dot{x} < 0$	II → RI	$x > r$,	$\dot{x} = 0$
RI → VIII	$x = x_{\text{RI}} + (1-r)\left(1 + \frac{\xi\delta}{\epsilon-\delta}\right)$,	$\dot{x} > 0$	RI → II	$x = x_{\text{RI}}$,	$\dot{x} < 0$
II → III	$x = r$,	$\dot{x} < 0$	III → IV	$x = -1$,	$\dot{x} < 0$
V → VI	$x = x_{\text{V}} + (1-r)\left(1 + \frac{\xi\delta}{\epsilon-\delta}\right)$,	$\dot{x} > 0$	IV → V	$x > -\lambda$,	$\dot{x} = 0$
V → IV	$x = x_{\text{V}}$,	$\dot{x} < 0$	IV → X	$x = -\lambda$,	$\dot{x} < 0$
X → VI	$x = -\lambda + \frac{\epsilon(1-r)}{\epsilon-\delta}$,	$\dot{x} > 0$	VI → RV	$x < -r$,	$\dot{x} = 0$
RV → IV	$x = x_{\text{RV}} - (1-r)\left(1 + \frac{\xi\delta}{\epsilon-\delta}\right)$,	$\dot{x} < 0$	VI → VII (III)	$x = -r$,	$\dot{x} > 0$
RV → VI	$x = x_{\text{RV}}$,	$\dot{x} > 0$	VII (III) → VIII	$x = 1$,	$\dot{x} > 0$
VIII → I	$x < \lambda$,	$\dot{x} = 0$	I → VIII	$x = x_{\text{I}}$,	$\dot{x} > 0$
I → II	$x = x_{\text{I}} - (1-r)\left(1 + \frac{\xi\delta}{\epsilon-\delta}\right)$,	$\dot{x} < 0$	VIII → IX	$x = \lambda$,	$\dot{x} > 0$

and the martensite volume fraction is computed by

$$\xi = \begin{cases} \dfrac{(\epsilon - \delta)\,(x_{\text{RI}} - r)}{\epsilon\,(\lambda - 1) - \delta\,(\lambda - r)}, & \text{RI} \\[2ex] -\dfrac{(\epsilon - \delta)\,(x_{\text{RV}} + r)}{\epsilon\,(\lambda - 1) - \delta\,(\lambda - r)}, & \text{RV}, \end{cases}$$

where x_{RI} and x_{RV} are the values of x at the time when state RI and RV are entered.

References

[1] S. Saadat, J. Salichs, M. Noori, Z. Hou, H. Davoodi, I. Bar-on, Y. Suzuki, A. Masuda, An overview of vibration and seismic applications of NiTi shape memory alloy, Smart Materials and Structures 11 (2) (2002) 218. `doi:0964-1726-11-2-305`.

[2] S. Seelecke, I. Muller, Shape memory alloy actuators in smart structures: Modeling and simulation, Applied Mechanics Reviews 57 (1) (2004) 23–46. `doi:10.1115/1.1584064`.

[3] L. G. Machado, D. C. Lagoudas, Nonlinear dynamics of a SMA passive vibration damping device, in: Smart Structures and Materials 2006: Damping and Isolation, Vol. 6169, 2006, pp. 6169X1–6169X12. `doi:10.1117/12.658062`.

[4] O. E. Ozbulut, S. Hurlebaus, R. Desroches, Seismic Response Control Using Shape Memory Alloys: A Review, Journal of Intelligent Material Systems and Structures 22 (14) (2011) 1531–1549. `doi:10.1177/1045389X11411220`.

[5] J. M. Jani, M. Leary, A. Subic, M. A. Gibson, A review of shape memory alloy research, applications and opportunities, Materials & Design (1980-2015) 56 (2014) 1078–1113. `doi:10.1016/j.matdes.2013.11.084`.

[6] D. Bernardini, T. J. Pence, Models for one-variant shape memory materials based on dissipation functions, International Journal of Non-Linear Mechanics 37 (8) (2002) 1299–1317. `doi:10.1016/S0020-7462(02)00020-3`.

[7] C. Morin, Z. Moumni, W. Zaki, A constitutive model for shape memory alloys accounting for thermomechanical coupling, International Journal of Plasticity 27 (5) (2011) 748–767. `doi:10.1016/j.ijplas.2010.09.005`.

[8] D. Lagoudas, D. Hartl, Y. Chemisky, L. Machado, P. Popov, Constitutive model for the numerical analysis of phase transformation in polycrystalline shape memory alloys, International Journal of Plasticity 32–33 (2012) 155–183. `doi:10.1016/j.ijplas.2011.10.009`.

[9] E. J. Graesser, F. A. Cozzarelli, Shape Memory Alloys as New Materials for Aseismic Isolation, Journal of Engineering Mechanics 117 (11) (1991) 2590–2608. `doi:10.1061/(ASCE)0733-9399(1991)117:11(2590)`.

[10] Z. C. Feng, D. Z. Li, Dynamics of a Mechanical System with a Shape Memory Alloy Bar, Journal of Intelligent Material Systems and Structures 7 (4) (1996) 399–410. `doi:10.1177/1045389X9600700404`.

[11] M. A. Savi, P. M. Pacheco, A. M. Braga, Chaos in a shape memory two-bar truss, International Journal of Non-Linear Mechanics 37 (8) (2002) 1387–1395. `doi:10.1016/S0020-7462(02)00029-X`.

[12] L. G. Machado, M. A. Savi, P. M. C. Pacheco, Nonlinear dynamics and chaos in coupled shape memory oscillators, International Journal of Solids and Structures 40 (19) (2003) 5139–5156. `doi:10.1016/S0020-7683(03)00260-9`.

[13] M. A. Savi, Nonlinear dynamics and chaos in shape memory alloy systems, International Journal of Non-Linear Mechanics 70 (2015) 2–19. `doi:10.1016/j.ijnonlinmec.2014.06.001`.

[14] S. Seelecke, Modeling the dynamic behavior of shape memory alloys, International Journal of Non-Linear Mechanics 37 (8) (2002) 1363–1374. `doi:10.1016/S0020-7462(02)00030-6`.

[15] D. Bernardini, F. Vestroni, Non-isothermal oscillations of pseudoelastic devices, International Journal of Non-Linear Mechanics 38 (9) (2003) 1297–1313. `doi:10.1016/S0020-7462(02)00065-3`.

[16] W. Lacarbonara, D. Bernardini, F. Vestroni, Nonlinear thermomechanical oscillations of shape-memory devices, International Journal of Solids and Structures 41 (5) (2004) 1209–1234. `doi:10.1016/j.ijsolstr.2003.10.015`.

[17] Y. Ivshin, T. J. Pence, A Thermomechanical Model for a One Variant Shape Memory Material, Journal of Intelligent Material Systems and Structures 5 (4) (1994) 455–473. `doi:10.1177/1045389X9400500402`.

[18] D. Bernardini, G. Rega, Evaluation of different sma models performances in the nonlinear dynamics of pseudoelastic oscillators via a comprehensive modeling framework, International Journal of Mechanical Sciences 130 (2017) 458–475. doi:10.1016/j.ijmecsci.2017.06.023.

[19] V. Piccirillo, J. M. Balthazar, B. R. Pontes, Analytical study of the nonlinear behavior of a shape memory oscillator: Part i—primary resonance and free response at low temperatures, Nonlinear Dynamics 59 (4) (2010) 733–746. doi:10.1007/s11071-009-9573-1.

[20] V. Piccirillo, J. Balthazar, A. Tusset, D. Bernardini, G. Rega, Non-linear dynamics of a thermomechanical pseudoelastic oscillator excited by non-ideal energy sources, International Journal of Non-Linear Mechanics 77 (2015) 12–27. doi:10.1016/j.ijnonlinmec.2015.06.013.

[21] D. Lagoudas, L. Machado, M. Lagoudas, Nonlinear Vibration of a One-Degree of Freedom Shape Memory Alloy Oscillator: A Numerical-experimental Investigation, in: 46th AIAA/ASME/ASCE/AHS/ASC Structures, Structural Dynamics and Materials Conference, 2005, pp. 1–18. doi:10.2514/6.2005-2119.

[22] L. G. Machado, Shape memory alloys for vibration isolation and damping, Ph.D. thesis, Texas A&M University (2007).

[23] L. G. Machado, D. C. Lagoudas, M. A. Savi, Lyapunov exponents estimation for hysteretic systems, International Journal of Solids and Structures 46 (6) (2009) 1269–1286. doi:10.1016/j.ijsolstr.2008.09.013.

[24] M. O. Moussa, Z. Moumni, O. Doaré, C. Touzé, W. Zaki, Non-linear dynamic thermomechanical behaviour of shape memory alloys, Journal of Intelligent Material Systems and Structures 23 (14) (2012) 1593–1611. doi:10.1177/1045389X12448446.

[25] O. Doaré, A. Sbarra, C. Touzé, M. O. Moussa, Z. Moumni, Experimental analysis of the quasi-static and dynamic torsional behaviour of shape memory alloys, International Journal of Solids and Structures 49 (1) (2012) 32–42. doi:10.1016/j.ijsolstr.2011.09.009.

[26] M. Xia, Q. Sun, Jump phenomena of rotational angle and temperature of NiTi wire in nonlinear torsional vibration, International Journal of Solids and Structures 56–57 (2015) 220–234. doi:10.1016/j.ijsolstr.2014.11.002.

[27] M. Xia, Q. Sun, Thermomechanical responses of nonlinear torsional vibration with NiTi shape memory alloy—-Alternative stable states and their jumps, Journal of the Mechanics and Physics of Solids 102 (2017) 257—276. doi:10.1016/j.jmps.2016.11.015.

[28] M. Xia, Q. Sun, Grain size effects on stability of nonlinear vibration with nanocrystalline NiTi shape memory alloy, Smart Materials and Structures 26 (10) (2017) 105033–105043. doi:0964-1726/26/i=10/a=105033.

[29] S. Jose, G. Chakraborty, R. Bhattacharyya, Coupled thermo-mechanical analysis of a vibration isolator made of shape memory alloy, International Journal of Solids and Structures 115–116 (2017) 87–103. `doi:10.1016/j.ijsolstr.2017.03.001`.

[30] P. Thamburaja, A finite-deformation-based phenomenological theory for shape-memory alloys, International Journal of Plasticity 26 (8) (2010) 1195–1219. `doi:10.1016/j.ijplas.2009.12.004`.

[31] T. K. Caughey, Sinusoidal Excitation of a System With Bilinear Hysteresis, Journal of Applied Mechanics 27 (4) (1960) 640–643. `doi:10.1115/1.3644075`.

[32] T. Kalmár-Nagy, A. Shekhawat, Nonlinear dynamics of oscillators with bilinear hysteresis and sinusoidal excitation, Physica D: Nonlinear Phenomena 238 (17) (2009) 1768–1786. `doi:10.1016/j.physd.2009.06.016`.

[33] A. Ahadi, Q. Sun, Stress hysteresis and temperature dependence of phase transition stress in nanostructured NiTi—–Effects of grain size, Applied Physics Letters 103 (2) (2013) 021902. `doi:10.1063/1.4812643`.

[34] A. Ahadi, Q. Sun, Effects of grain size on the rate-dependent thermomechanical responses of nanostructured superelastic NiTi, Acta Materialia 76 (2014) 186–197. `doi:10.1016/j.actamat.2014.05.007`.

[35] Q. Sun, Effects of grain size on phase transition behavior of nanocrystalline shape memory alloys, Science China Technological Sciences 57 (4) (2014) 671–679. `doi:10.1007/s11431-014-5505-5`.

[36] A. Ahadi, Q. Sun, Stress-induced nanoscale phase transition in superelastic NiTi by in situ X-ray diffraction, Acta Materialia 90 (2015) 272–281. `doi:10.1016/j.actamat.2015.02.024`.

[37] C. Cisse, W. Zaki, T. B. Zineb, A review of constitutive models and modeling techniques for shape memory alloys, International Journal of Plasticity 76 (2016) 244–284. `doi:10.1016/j.ijplas.2015.08.006`.

[38] H. Yin, Y. He, Q. Sun, Effect of deformation frequency on temperature and stress oscillations in cyclic phase transition of NiTi shape memory alloy, Journal of the Mechanics and Physics of Solids 67 (2014) 100–128. `doi:10.1016/j.jmps.2014.01.013`.

[39] Y. Liu, Z. Xie, J. V. Humbeeck, L. Delaey, Asymmetry of stress–strain curves under tension and compression for NiTi shape memory alloys, Acta Materialia 46 (12) (1998) 4325–4338. `doi:10.1016/S1359-6454(98)00112-8`.

[40] M. Abramowitz, I. A. Stegun, et al., Handbook of mathematical functions: with formulas, graphs, and mathematical tables, Vol. 55, Dover New York, 1972.

[41] P. Blanchard, R. Devaney, G. Hall, Differential Equations, Cengage Learning, 2012.

[42] W. Thomson, Theory of vibration with applications, Prentice Hall, 1997.

[43] A. H. Nayfeh, D. T. Mook, Nonlinear oscillations, John Wiley & Sons, 2008.